Geometric phases in soft materials

Abbaszadeh, H.

Chapter 3.

Photonic waveguides in liquid crystals

Liquid crystals are soft matter phases characterized by their orientational order [141]. As a result of this order, liquid crystals can control the propagation of light in a reconfigurable way, with applications ranging from liquid crystal displays (LCD) [125] to adaptive lenses [12]. Light waves that propagate through a birefringent material such as a liquid crystal acquire a Pancharatnam-Berry phase. We have seen in the first chapter of this thesis that a spatially varying Pancharatnam-Berry phase has an effect similar to a change of the refractive index in the form of a generalized Snell's law, Eq. 1.11 and interferes with the defraction of light beams [40]. Therefore, light incident to a birefringent medium can change direction, even when the refractive index of the medium is homogeneous [5, 7].

Light beams acquire a geometric Pancharatnam-Berry phase when passing through a thin film of birefringent molecules [118, 131]. Therefore, as we have seen in the first chapter, subwavelength liquid crystal metasurfaces can be designed to scatter a light beam towards a certain direction, making these materials suitable for flat optics elements [84, 93]. Furthermore, recently developed plasmonic photopatterning techniques [22, 51] can be used to achieve control over the patterns of the nematic textures in thin liquid crystal polymers, paving the way to achieve various optical performances using these materials [24, 28]. These techniques are used for designing and manufacturing of geometric phase lenses [120] and achieving a controlled continuous profile of the Pancharatnam-Berry phase [23]. In this chapter, we study the propagation of light in a liquid crystal medium with a particular focus on the waveguiding regimes in these materials.

Optical waveguides, i.e. electromagnetic waveguides at optical frequencies, have been realized in a number of ways, including using spatial gradients in the refractive index [128] and using photonic bandgaps [114, 136]. The examples include graded index fibers [168] and photonic crystal fibers [124, 139]. However, all these methods are based on changing the refractive index of the medium, e.g. through laser writing the dielectric material or by using optical cavities, such as in photonic crystal fibers. Slussarenko *et al.* [56] observed such waveguiding regimes by using consecutive geometric phase lenses of liquid crystals. In this chapter, we generalize this work by presenting a theoretical framework to study the guided modes in a liquid crystal. The analysis in this chapter will provide the basis for a discussion of topological photonics in liquid crystals which we will follow in the next chapter.

We study the paraxial light propagation (i.e. at small angles with the direction of propagation) in a birefringent medium that is described by a Schrödinger-type equation with the distance along the propagation direction as an effective time [104, 108]. A spatial modulation of the director field introduces a time-dependent vector and scalar potential into this effective theory. We will study a specific pattern that is periodic with the same length scale as the periodicity of the ordinary and extraordinary polarized light dynamics [141]. We focus on the regime where the orientational variations of the molecules happen in a scale that is smaller than the defocusing length of the light beam which leads to a separation of the scales in the dynamics of light wavepacket from smaller scale variations. This slow dynamics is then mapped to the dynamics of a quantum wavefunction under a time-periodic Hamiltonian which are studied using Floquet theory [61, 79]. We then use the techniques of the Floquet quantum mechanics to derive a numerical scheme to determine the guided modes of the medium in such regimes. We also show the resemblance of the birefringence effect with a variation of the refractive index by studying curved liquid crystal waveguides what reminds one to an optical fiber [128].

3.1 Paraxial light propagation in uniaxial media

Consider the propagation of a Gaussian light beam in a uniform uniaxial medium where the nematic molecules are oriented along the plane orthogonal to the direction of propagation. We start by Helmholtz equations for the transverse electromagnetic (TEM, $E_z = B_z = 0$) waves,

$$\frac{\partial^2}{\partial z^2}\boldsymbol{\psi}_{\mathrm{xy}} = -\nabla_\perp^2 \boldsymbol{\psi}_{\mathrm{xy}} - k_0^2 \boldsymbol{\epsilon}\boldsymbol{\psi}_{\mathrm{xy}}, \tag{3.1}$$

where $\boldsymbol{\psi}_{\mathrm{xy}} = (E_x, E_y)$ is the transverse electric field, k_0 is the light wavenumber in the free space, and $\boldsymbol{\epsilon}$ is the dielectric of the medium. In liquid crystals, because of the shape of the nematic molecules, beams with different polarizations experience different refractive indices. In such so-called uniaxial media, the dielectric tensor is given by

$$\boldsymbol{\epsilon}(x, y, z) = \epsilon_\perp \mathbf{I} + (\epsilon_\parallel - \epsilon_\perp)\mathbf{n}^T\mathbf{n}, \tag{3.2}$$

where $\epsilon_\perp$ and $\epsilon_\parallel$ are the components of the dielectric tensor along the ordinary and extraordinary axes of the molecules, respectively and $\mathbf{n}(x, y, z)$ is the director field of the nematic orientations. The refractive indices for these two axes are combined in the following matrix:

$$\mathbf{N} = \sqrt{\boldsymbol{\epsilon}_D} = \mathrm{diag}(n_{\mathrm{o}}, n_{\mathrm{e}}), \tag{3.3}$$

where $\boldsymbol{\epsilon}_D = \mathrm{diag}(\epsilon_\perp, \epsilon_\parallel)$ is the diagonalized dielectric tensor. Thus, the uniaxial medium is characterized by two particular indices n_{o} and n_{e}, that correspond to the so-called ordinary and extraordinary polarizations that propagate unchanged. Therefore, three characteristic length scales naturally appear: the light wavelength λ, the beating length $\Lambda = \lambda/(n_{\mathrm{e}} - n_{\mathrm{o}})$ between the ordinary and extraordinary polarizations, and the Rayleigh length Z_{R} that determines the size of the Gaussian beam given in terms of the beam's wavelength and its width, w by

$$Z_{\mathrm{R}} = \pi \bar{n} w^2/\lambda, \tag{3.4}$$

where $\bar{n} = (n_{\mathrm{e}} + n_{\mathrm{o}})/2$. Additional length scales characterize the spatial pattern of the liquid crystal. Here, we focus on patterns where only the orientation of the nematic liquid crystal molecules (i.e. the director field) is changed, while the ordinary and extraordinary indices n_{o} and n_{e} are the same in the whole system. For a liquid crystal composed of uniaxial elements

with orientations in the xy-plane, which is the case that is considered in this thesis, the director field is determined in terms of a single parameter, θ, as $\mathbf{n} = (-\sin\theta, \cos\theta, 0)$, where θ is the angle between the extraordinary and the y axes, see Fig. 3.1. The ordinary-extraordinary frame is rotated with respect to the Cartesian coordinates with the angle θ that corresponds to the orientation of the molecules. Therefore, one can rewrite Eq. 3.1 for the ordinary-extraordinary waves using the substitution $\boldsymbol{\psi}_{\text{oe}} = \mathbf{R}^{-1}(\theta)\boldsymbol{\psi}_{\text{xy}}$, where $\mathbf{R}(\theta)$ is the rotation operator with angle θ, and obtain

$$\begin{aligned}\partial_z^2\boldsymbol{\psi}_{\text{oe}} - 2i(\partial_z\theta)\sigma_y\partial_z\boldsymbol{\psi}_{\text{oe}} &= -\nabla_\perp^2\boldsymbol{\psi}_{\text{oe}} \\ &+ 2i(\nabla_\perp\theta)\sigma_y\cdot\nabla_\perp\boldsymbol{\psi}_{\text{oe}} + i(\nabla^2\theta)\sigma_y\boldsymbol{\psi}_{\text{oe}} \\ &+ (\nabla\theta)^2\boldsymbol{\psi}_{\text{oe}} - k_0^2\boldsymbol{\epsilon}_D\boldsymbol{\psi}_{\text{oe}}.\end{aligned} \tag{3.5}$$

We now present the regimes in which the dynamic of a wavepacket can be separated from the variations in small scales using slowly varying envelope approximation (SVEA). These regimes are determined by the relative ratios of the length scales that are discussed above. More precisely, we assume that between these scales, λ is usually the smallest (or fastest), but for the other two length scales various situations could take place, depending on the ratio

$$\frac{\Lambda}{Z_{\text{R}}} = \frac{(\lambda/Z_{\text{R}})^2}{\pi\bar{n}\Delta n}. \tag{3.6}$$

In the following, we study the large birefringence regime, where the light focusing can be affected from the dynamics inside each beating length. The small birefringence regimes are discussed in the appendix 3.5.1.

3.1.1 Large birefringent medium: interaction picture

When the birefringence of the medium, $\Delta n = n_{\text{e}} - n_{\text{o}}$ is sufficiently large, we are in a regime where Λ is a fast variable compared to the Rayleigh length, Z_{R} as given by Eq. 3.4. Thus, there are two small quantities

$$\varepsilon_1 = \lambda/Z_{\text{R}} \qquad \text{and} \qquad \varepsilon_2 = \Lambda/Z_{\text{R}} \tag{3.7}$$

concerning the paraxial light propagation in this regime. In such case, the effect of changes happening over length Z_{R} can be considered as perturbations on top of the faster dynamics which takes place over the birefringence wavelength Λ. This z-dependent interaction can be treated by separating the dynamics over the fast and slow length scales, similar to exploiting the interaction picture in

quantum mechanics [45]. This is done by writing down the wavefunction as $\boldsymbol{\psi}_{\text{oe}}(x, y, z, \varepsilon_1 z, \varepsilon_2 z) = \mathbf{U}_{\text{oe}}(z, \varepsilon_2 z)\psi(x, y, z, \varepsilon_1 z)$, where

$$\mathbf{U}_{\text{oe}}(z) = e^{ik_0 \mathbf{N} z} \tag{3.8}$$

is the evolution of the polarization in a homogeneous uniaxial medium. The dynamical equation for the wavepacket in the interaction picture can be cast as

$$\begin{aligned}\partial_z^2 \psi + \left[2ik_0\mathbf{N} - 2i(\partial_z\theta)\mathbf{S}(z)\right]\partial_z\psi &= -\nabla_\perp^2\psi \\ &- 2k_0(\partial_z\theta)\mathbf{S}(z)\mathbf{N}\psi + 2i(\nabla_\perp\theta)\mathbf{S}(z)\cdot\nabla_\perp\psi \\ &+ i(\nabla^2\theta)\mathbf{S}(z)\psi + (\nabla\theta)^2\psi,\end{aligned} \tag{3.9}$$

where

$$\mathbf{S}(z) = \mathbf{U}_{\text{oe}}^{-1}(z)\sigma_y\mathbf{U}_{\text{oe}}(z) = e^{i\frac{2\pi z}{\Lambda}\sigma_z}\sigma_y \tag{3.10a}$$

$$= \sigma_y\cos(k_0\Delta n z) + \sigma_x\sin(k_0\Delta n z) \tag{3.10b}$$

is the spin-dependent part of the the dynamics in terms of the Pauli matrices. To see how the terms involved in this equation are compared to each other, we write them in terms of dimensionless variables $X = x/w$, $Y = y/w$, and $Z = z/Z_{\text{R}}$ and then multiply the entire equation by $\dfrac{Z_{\text{R}}}{2\bar{n}k_0} = \dfrac{w^2}{4}$ to get

$$\begin{aligned}\frac{\varepsilon_1}{4\pi\bar{n}}\partial_Z^2\psi + \left[i\frac{\mathbf{N}}{\bar{n}} - \frac{i}{2\pi\bar{n}}\varepsilon_\theta(\partial_{Z_\theta}\theta)\mathbf{S}(z/\Lambda)\right]\partial_Z\psi \\ = -\frac{1}{4}\nabla_{\tilde{\perp}}^2\psi - (Z_{\text{R}}/Z_\theta)(\partial_{Z_\theta}\theta)\mathbf{S}(z/\Lambda)\frac{\mathbf{N}}{\bar{n}}\psi \\ + \frac{i}{2}(\nabla_{\tilde{\perp}}\theta)\mathbf{S}(z/\Lambda)\cdot\nabla_{\tilde{\perp}}\psi \\ + \frac{i}{4}\left[\nabla_{\tilde{\perp}}^2\theta + (w/Z_\theta)^2\partial_{Z_\theta}^2\theta\right]\mathbf{S}(z/\Lambda)\psi \\ + \frac{i}{4}\left[\left(\nabla_{\tilde{\perp}}\theta\right)^2 + (w/Z_\theta)^2\left(\partial_{Z_\theta}\theta\right)^2\right]\mathbf{S}(z/\Lambda)\psi,\end{aligned} \tag{3.11}$$

where $\nabla_{\tilde{\perp}}$ is the gradient with respect to dimensionless variables and Z_θ is a charactristic length scale over which the orientation of the molecules vary along the z axis, and $\varepsilon_\theta = \lambda/Z_\theta$. Assuming $\lambda \ll Z_\mathrm{R}$ which implies $w \ll Z_\mathrm{R}$ leads to the following dynamical equation after reviving the original variables:

$$\begin{aligned} i\partial_z\psi = &-\frac{1}{2\bar{n}k_0}\nabla_\perp^2\psi - (\partial_z\theta)\mathbf{S}(z)\psi \\ &+ \frac{i}{\bar{n}k_0}(\nabla_\perp\theta)\mathbf{S}(z)\cdot\nabla_\perp\psi + \frac{i}{2\bar{n}k_0}(\nabla^2\theta)\mathbf{S}(z)\psi \\ &+ \frac{1}{2\bar{n}k_0}(\nabla\theta)^2\psi, \end{aligned} \tag{3.12}$$

which can be rearranged into the following form:

$$\begin{aligned} i\partial_z\psi = &-\frac{1}{2\bar{n}k_0}\left[\nabla_\perp - i(\nabla_\perp\theta)\mathbf{S}(z)\right]^2\psi - (\partial_z\theta)\mathbf{S}(z)\psi \\ &+ \frac{1}{2\bar{n}k_0}\left[i(\partial_z^2\theta)\mathbf{S}(z) + (\partial_z\theta)^2\right]\psi. \end{aligned} \tag{3.13}$$

The last two terms are of order $\frac{1}{Z_\mathrm{R}}\left(\frac{w}{Z_\theta}\right)^2$, and therefore can be neglected in the limit where $w \ll Z_\theta$. This leads to the wavepacket evolution

$$i\,\frac{\partial\psi}{\partial z} = -\frac{1}{2\bar{n}k_0}\left[\nabla_\perp + i\mathbf{A}\right]^2\psi + \mathbf{V}\psi, \tag{3.14}$$

with $\mathbf{A}(z) = -(\nabla_\perp\theta)\mathbf{S}(z)$ and $\mathbf{V}(z) = -(\partial_z\theta)\mathbf{S}(z)$, where $\mathbf{S}(z)$ is a z-dependent matrix that only depends on Λ and is responsible for the polarization dynamics. Formally, this equation resembles the Schrödinger equation of quantum mechanics, provided that the paraxial direction z is replaced by time. From now on, in this chapter and the next one we refer to z as time.

3.2 Guiding regimes for light in a uniaxial medium

We now use the results in the previous section to study the photonic guiding regimes in liquid crystals as a result of the interplay between light and the director of the nematic molecules.

In the quantum mechanical language, a guided mode to the paraxial equation of motion, Eq. 3.14 is an eigenmode of the Hamiltonian, if it does not depend on time. However, note that since in this effective Schrodinger equation the Hamiltonian is time-dependent, and therefore, it is not generally

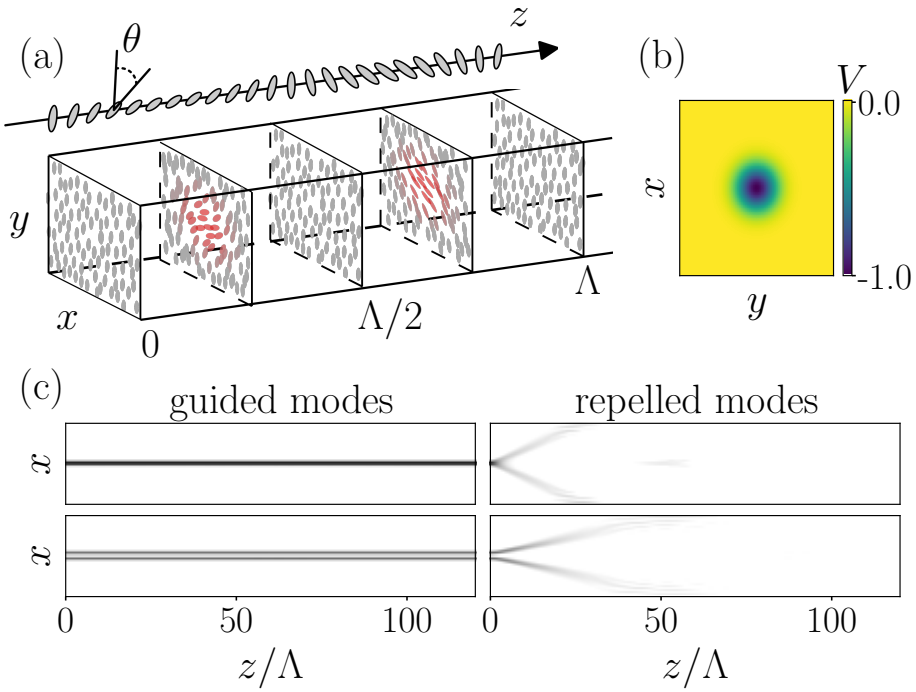

Figure 3.1: (a) The liquid crystal configuration corresponding to one waveguide, Eq. 3.16 with $\Gamma_0 = \pi/12$ and $w_p = 1$ and (b) the effective potential associated with it. Left panels in (c) and show the evolution of the guided modes while right panels correspond to the repelled modes of this system. Top and bottom panels in (c) correspond to the zeroth and first order modes of the system.

possible to find an eigenmode of the evolution for the entire period of time. This time dependence comes from two sources of drive: the phase evolution $\mathbf{U}_{\text{oe}}$ and the periodicity of the configuration along the z-direction. When the orientation $\theta(x, y, z)$ of the director field is periodic in the paraxial direction z with a the same period Λ of the phase evolution, the Hamiltonian is Λ-periodic in z, and can be analyzed using Floquet theory [61, 79]. The main idea is that the propagation of light over large distances $z \gg \Lambda$ is essentially captured by repeating its evolution over one period Λ, which is described by the evolution operator $U(\Lambda)$ associated with equation (3.14). The eigenvalues of the operator $U(\Lambda)$ are phases of the form $\mathrm{e}^{-\mathrm{i}\kappa\Lambda}$ where κ is the quasi-momentum in the paraxial direction of the corresponding eigenmode. Here, the eigenmodes describe guided modes of the soft waveguide, and up to variations at the (small) scale Λ their intensity remains constant.

The use of Floquet eigenmodes generalizes the previously used methods in finding the eigenmodes of the time-averaged Hamiltonian [56]. A perturbative approach can be used to find the dynamics inside a Floquet period using quasi-modes as an approximation for the Floquet-Bloch modes [40, 182]. Here, we use a more general approach that is based on finding the eigenmodes of the system's evolution in the stroboscopic picture. Using this new method, one can also find the higher-order guided modes of such systems, i.e. modes that repeat themselves (up to a global phase), but with a different quasi-momentum and intensity pattern. Also, the eigenmodes of the Floquet evolution operator will remain guided over larger distances in z, given the other sources of losses are not there ♠.

We construct this evolution operator numerically by slicing period Λ into small steps δz and by using the following feature of the evolution operator:

$$U(z_3, z_2)U(z_2, z_1) = U(z_3, z_1). \tag{3.15}$$

Since $U(\Lambda)$ is a unitary operator, its eigenvalues reside on the unit circle. Hence, unlike a usual quantum problem, a highly oscillating mode in this spectrum can lie very close to another mode that is well localized in its spatial pattern. This makes the numerical diagonalization of this operator unstable and subject to accidental degeneracies. We solve this issue by exploiting the Sambe space representation of the Floquet Hamiltonian and their modes, which we explain in the appendix 3.5.3.

We applied this method to a few systems. Here, we show the calculations that reproduce the results by Ref. [56]. We consider a Gaussian nematic director patterning that is described by the following orientational field:

$$\theta(x, y, z) = \Gamma_0 e^{-(x^2+y^2)/w_p^2} \sin(2\pi z/\Lambda), \tag{3.16}$$

where $\Gamma_0 = \pi/12$ is the amplitude of the director field's rotation, w_p is the width of the Gaussian pattern, and Λ the periodicity of the pattern along the effective time and is equal to the beating length between the ordinary and extraordinary light beams. The refractive indices for this birefringent medium are $n_o = 1.5$ and $n_e = 1.7$ and thus we have $\Lambda = \lambda/\Delta n = 5\lambda$. We also consider $w_p = \lambda$. The liquid crystal pattern associated with this pattern is shown in Fig. 3.1(a).

♠In this study we do not consider the internal sources of loss that can give rise due to the interaction of the electromagnetic waves with a liquid crystal. We will discuss this in more detail in a discussion about non-Hermiticity of this system in the next chapter.

We use our numerical methods to generalize the results of the Ref. [56] by finding the various guided modes with different spatial intensity pattern. We order these modes by the first moment of their spatial distribution around the waveguide center, $\frac{1}{\mathcal{N}}\int rI(r)dr$, where $I(r) = \psi^\dagger(r)\psi(r)$ is the light intensity and is non-negative everywhere, and $\mathcal{N} = \int I(r)dr$ is the normalization factor. The evolution of the first two guided modes obtained with this method is shown in the left panels of the Fig. 3.1(c). With each guided mode is associated a repelled mode obtained by its complex conjugation. To understand why this is the case, we note that in our numerical method we build a $2N \times 2N$ matrix for $U(\Lambda)$, where N is the size of the mesh in the simulation box in each of the x- and y directions, and the doubling factor comes from the polarization degree of freedom. However, the guided modes of a waveguide can not span the entire vector space of the initial modes, as not all the modes are guided by this waveguide. We note that the eigenvectors of the evolution operator come in pairs of modes with similar intensity patterns, of which one is a physical mode that corresponds to a guided mode of the evolution. The other mode in each pair is unphysical, i.e. their polarization components oscillate with the grid. Thus, the doubling of the degrees of freedom in this numerical scheme leads to spurious modes to construct half of the spectrum. Instead of these unphysical modes, the system supports the presence of repelled modes, which in the Ref. [56] are the modes with opposite circular polarizations of the guided modes. In our numerical scheme here, the complex conjugation does this transformation in the polarization. The complex conjugated modes correspond to the eigenmodes of a new Hamiltonian which has a scalar potential with opposite sign. This change in the sign leads to the transformation from a potential well to a potential barrier for the guided modes of the initial system in the effective picture. In Fig. 3.1 (c) we show two guided modes and the repelled modes associated to them.

3.3 Curved waveguides

We saw in the first chapter that the Snell's law, Eq. 1.11, in the presence of the birefringent medium acquires a modifying term that is proportional to the gradient of the Pancharatnam-Berry phase of the light beam. Therefore, the liquid crystal optical waveguides that we described in the previous section might also be seen as a consequence of the similar effect of the spatial variation in the Pancharatnam-Berry phase with the refractive index grading of the medium. Here, we present a test of this comparison by studying the liquid

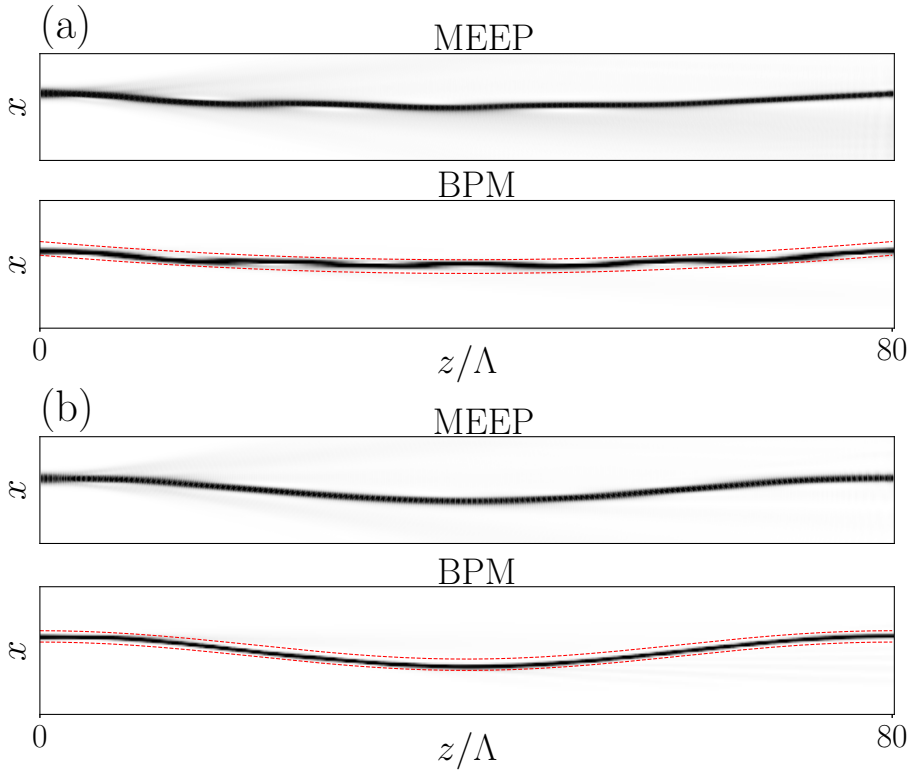

Figure 3.2: Curved (a) parabolic and (b) sinusoidal waveguides. The results from solving Maxwell's equations using the software MEEP and solving the effective Schrödinger equations using BPM methods show agreement. Dashed lines correspond to the waveguide borders, i.e. the width of the transverse Gaussian patterns that create them.

crystal waveguides with curvature. These curved waveguides can be useful when for example a time-varying coupling strength of the waveguides is needed. This will allow us to investigate the phenomena associated with tight-binding quantum systems with time-varying hopping amplitudes, once we develop this framework in the next chapter.

More importantly, the curvature can lead to a new coupling between the polarization of light and its path via a spin-orbit coupling [60, 110, 111]. Light beam inside these waveguides acquire both Pancharatnam-Berry phase and Rytov-Vladimirskii-Berry phase simultaneously, see § 1.2. The interplay of theses two different geometric phases and the phenomena associated to this interplay are subjects to future investigations.

For the numerical study of these systems we use both MEEP software [102] as well as a beam propagation method (BPM) in Python. MEEP solves the full Maxwell's equations using finite-difference time-domain (FDTD) method which makes it numerically expensive for large-scale systems. The BPM method uses the slowly varying envelope approximation and the resulting first order differential equation along the z-axis to solve this system as an initial value problem. Using the paraxial equation of motion, Eq. 3.14, we develope a code based on the Crank-Nicolson method to solve this equation with a given initial condition. The latter is a considerably computationally faster code for larger-scale systems, such as those we consider for a lattice of waveguides in the next chapter. The Schrödinger solver code can also be adapted to solve the Floquet propagators and their diagonalization to find the guided modes, as we discuss in appendix 3.5.3.

We observe that similar to before, for a small curvatures in the waveguide shapes, the lights are guided for a specific circular polarized light, whereas the light beam with opposite polarization is completely repelled. The numerical results for the propagation of a guided mode (that is obtained in the previous section for a straight waveguide) inside a curved waveguide is shown in Fig. 3.2. These results also show a good agreement of our python code with the MEEP simulations.

We further notice an effect similar to reflection of light from waveguide walls in optical fibers [132], for example in Fig. 3.2. This is remarkable, since there is not a solid wall like in a index-graded optical fiber and shows a strong evidence to the generalized Snell's law, 1.11. This bouncing effect makes it important to have a bound on how much these waveguides can be curved so that the incident light is not transmitted outside. We further confirm this in Fig. 3.3 for a waveguide that has the sinusoidal shape with a curvature that is two times larger from the waveguide in Fig. 3.2(b).

3.4 Fully rotating nematic waveguides

So far we considered modulations of the nematic fields that are non-monotonic along the z direction, for example by the orientation that is spatially varied as

$$\theta(x, y, z) = \theta_0(x, y) \sin 2\pi z/\Lambda. \tag{3.17}$$

This consideration was done to achieve a smooth director field that is periodic along the z-axis. However, since θ is an orientation, it can also be periodic when it fully rotates on a cycle. Here, we consider a pattern that is periodic while we require the center of the waveguides to fully rotate. A full rotation

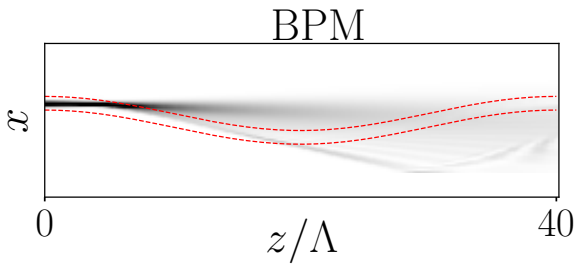

Figure 3.3: The effect of curvature in the ability of the waveguides we study for light confinement. We observe the coinciding light is transmitted outside when the waveguide curvature is twice as the one depicted in Fig. 3.2(b).

of the nematic pattern introduces a handedness which can be mapped to an effective time-reversal symmetry breaking in the paraxial limit, similar to the effect of a helical path [88]. However, as we discussed in our description of geometric phases of light, the nature of the rotation in the two problems above are different: in a fully rotating nematic waveguide this is a Pancharatnam-Berry phase, whereas in a helical waveguide it is a Rytov-Vladimirskii-Berry phase, resulting from a change in the orientation along the orbital path of the light beam.

Since the orientation of the molecules have a spatial dependent amplitude, e.g. in our first example in 3.16 that is given by

$$\theta_0(x, y) = \Gamma_0 \exp\left[-(x^2 + y^2)/w_p^2\right], \tag{3.18}$$

it is not possible to apply the full rotation in the entire xy-plane. In the example above, this can be seen by noticing the assymptotic behavior of the director field's orientation that vanishes at large distances from waveguide's center. Therefore, one needs to consider a fully rotating director field only in a finite region in the xy-plane. This full rotation at the center can be achieved by simply requiring that the director field continues in the same rotating manner after reaching its maximum (this can be achieved with $\Gamma_0 = \pi/2$ as well), as shown in Fig. 3.4(a). When $\Gamma_0 = \pi$, the center of the pattern reaches to its initial direction at $z = \Lambda/4$, but the nearby molecules are at their maximum rotation with an angle smaller than smaller than π. For the latter, the periodicity would still be achieved by the non-monotonic pattern suggested by Eq. 3.17.

As a result we can expect defects arising in the nematic texture due to this difference between the topology in the center and points far away. Consequently, a large gradient of the orientation is expected in the perpendicular plane. These defects can introduce large peaks in the gauge field around the discontinuity of the orientational order. To avoid large perturbations due to the discontinuity of the orientation along the xy-plane, we put these defects on a relatively far distance from the center of the waveguide. We consider the following pattern in a circle $C_R(0)$ around the center:

$$\theta_2 = \begin{cases} \theta_0(x,y)\sin\left(\frac{2\pi z}{\Lambda}\right) & \text{if } (x,y) \notin C_R(0) \text{ or } \frac{z}{\Lambda} \in [0, \frac{1}{4}] \\ 2\pi - \theta_0(x,y)\sin\left(\frac{2\pi z}{\Lambda}\right) & \text{if } (x,y) \in C_R(0) \text{ and } \frac{z}{\Lambda} \in [\frac{1}{4}, \frac{3}{4}] \\ 4\pi + \theta_0(x,y)\sin\left(\frac{2\pi z}{\Lambda}\right) & \text{if } (x,y) \in C_R(0) \text{ and } \frac{z}{\Lambda} \in [\frac{3}{4}, \frac{1}{4}] \\ \dots \end{cases} \tag{3.19}$$

This pattern is illustrated in Fig. 3.4(a). Note that R can essentially be large enough to make the discontinuity in the nematic orientation in the xy-plane negligible. However, now there are large gradients of the director field when passing through $z = \Lambda/4$ and $3\Lambda/4$ planes, see Fig. 3.4(b). To make this perturbation smaller, the Gaussian pattern $\theta(x,y)$ can be kept less sharp, i.e. wider. The width associated to the variations in the perpendicular plane can affect the validity of the paraxial approximation through changing the Rayleigh defocusing length.

With these considerations we now look at the guided modes of a fully rotating LC system in z. We use large R values for now, hence the entire nematic texture follows the modified variation Eq. 3.19. We observe that at $w_p \lessapprox 5$ the guided modes deviate largely from a Gaussian, but for more stretched patterns with larger width, we observe the guided modes that are close to a Gaussian pattern.

In conclusion, we have shown in this chapter that paraxial light propagation in a liquid crystal medium can be mapped to Floquet quantum mechanical systems. We then developed a numerical scheme to extract the guided modes in liquid crystals with beating length between ordinary and extraordinary lights much smaller than the defocusing length of the light beam. We used this numerical method to find guided photonic modes of a liquid crystal medium with certain nematic patterns. Our results include higher-order guided modes, guided modes in curved waveguides, and guided modes in fully rotating nematic patterns. Looking forward, we would like to investigate the interplay

between various geometric phases that a monochromatic light beam acquires in such waveguides. We will also discuss in the next chapter symmetries of these waveguides, which we will use towards implementation of topological photonics in designer liquid crystal media.

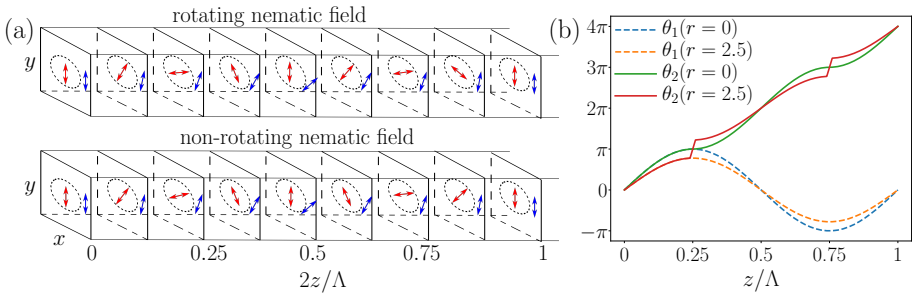

Figure 3.4: (a) Half a Floquet period of the liquid crystal configuration corresponding to rotating (top) and non-rotating (bottom) director fields. For clarity at each time step, one nematic for both inside and outside of the region C_R, depicted by the dashed circle, are shown. (b) The orientation field for rotating (solid lines) and non-rotating (dashed lines) at the center ($r = 0$) and one off-center, $r = 2.5$, point inside C_R. The full rotating director field at the center imposes discontinuity in the director field at off-center points inside C_R. We set $w_p = 5$ and $R = 15$ for this plot; larger pattern widths would lead to smaller discontinuity at $z/\Lambda = 0.25,\ 0.75$, but larger discontinuity in nematic orientation at the xy-plane when crossing from C_R.

3.5 Appendix

3.5.1 Dynamics of circularly polarized waves through a uniform uniaxial medium

In a uniform medium, where $\theta(x, y, z) = \theta_0$, the dielectric tensor is diagonalized as

$$\boldsymbol{\epsilon}_D = \mathbf{R}(\theta_0) \begin{pmatrix} \epsilon_\perp & 0 \\ 0 & \epsilon_\parallel \end{pmatrix} \mathbf{R}^{-1}(\theta_0), \tag{3.20}$$

where

$$\mathbf{R}(\theta) = \begin{pmatrix} \cos\theta & -\sin\theta \\ \sin\theta & \cos\theta \end{pmatrix}. \tag{3.21}$$

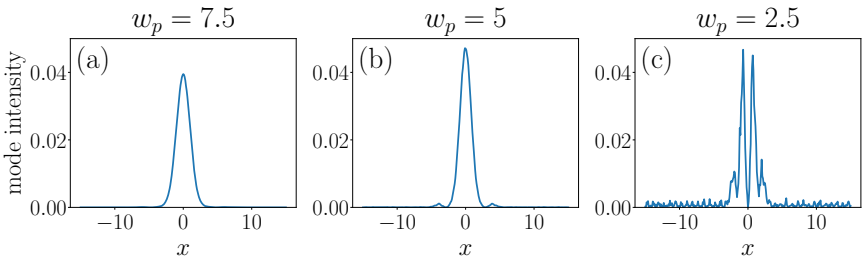

Figure 3.5: Floquet eigenmode of a fully rotating nematic waveguide for three values of the transverse pattern Gaussian widths. The narrower patterns correspond to larger discontinuities along the z direction, as depicted in Fig. 3.4(b). This discontinuity leads then to a deviation of the eigenmodes from Gaussian shapes. For these simulations we use $R = 15$.

Thus, the change of basis $\psi_{\text{oe}} = \mathbf{R}^{-1}(\theta_0)\psi_{\text{xy}}$ from Cartesian to ordinary/extraordinary (oe) basis diagonalizes the equation of motion 3.1. In the oe basis, the solution to the equation of motion is given by

$$\psi_{\text{oe}}(z) = \mathbf{U}_{\text{oe}}(z)\psi_{\text{oe}}(0) \tag{3.22}$$

where

$$\mathbf{U}_{\text{oe}} = \begin{pmatrix} e^{ik_0 n_o z} & 0 \\ 0 & e^{ik_0 n_e z} \end{pmatrix}, \tag{3.23}$$

where $n_o = \sqrt{\epsilon_\perp}$ and $n_e = \sqrt{\epsilon_\parallel}$ are refractive indices for ordinary and extraordinary lights, respectively.

Let us now consider propagation of a circularly polarized light in such a medium. We thus change our basis to left/right circularly polarized basis. The dynamics is then given by

$$\psi_{\text{L}}(z) = e^{i\bar{n}k_0 z}\left[\cos(\delta/2)\psi_{\text{L}}(0) - i\sin(\delta/2)e^{2i\theta_0}\psi_{\text{R}}(0)\right], \tag{3.24}$$

$$\psi_{\text{R}}(z) = e^{i\bar{n}k_0 z}\left[\cos(\delta/2)\psi_{\text{R}}(0) - i\sin(\delta/2)e^{-2i\theta_0}\psi_{\text{L}}(0)\right], \tag{3.25}$$

where $\bar{n} = (n_o + n_e)/2$ is the average refractive index and $\delta = k_0(n_e - n_o)z$ is the phase retardation via propagation. The length-scale corresponding to the polarization dynamics is then given by

$$\Lambda = 2\pi/(k_0\Delta n) = \lambda/\Delta n, \tag{3.26}$$

where $\Delta n = n_e - n_o$.

3.5.2 Dynamics of paraxial light propagation in liquid crystals with medium to low birefringence

In the chapter, we derived the dynamics of light wavepackets for a regime where $\Lambda \ll Z_{\mathrm{R}}$. We now focus on the intermediate values of the birefringence where the two length scales Λ and Z_{R} become of the same order, the light propagation dynamics enters a different regime where both of these length scales are slow compared to λ. Thus, the small quantities of the problem are

$$\varepsilon_1 = \lambda/Z_{\mathrm{R}}, \tag{3.27}$$

$$\varepsilon_2 = \lambda/\Lambda. \tag{3.28}$$

In this regime, we can not apply the interaction picture that is introduced above. Instead, the SVEA can directly be applied on the equation of motion Eq. (3.5). To do that, we start by expanding the wavefunction in the L/RCP basis as

$$\boldsymbol{\psi}_{\mathrm{oe}}(z) = F_{\mathrm{R}}(z)\psi_{\mathrm{R}} + F_{\mathrm{L}}(z)\psi_{\mathrm{L}}, \tag{3.29}$$

where $\psi_{\mathrm{R}} = \dfrac{1}{\sqrt{2}}(1; i)$ and $\psi_{\mathrm{L}} = \dfrac{1}{\sqrt{2}}(1; -i)$ are the eigenvectors of the Pauli matrix σ_y. Plugging this expansion into Eq. (3.5), we find the following set of coupled differential equations:

$$\begin{aligned}\partial_z^2 F_{\mathrm{R}}(z) - 2i(\partial_z\theta)\partial_z F_{\mathrm{R}}(z) = &-\nabla_\perp^2 F_{\mathrm{R}}(z) + 2i(\nabla_\perp\theta)\cdot\nabla_\perp F_{\mathrm{R}}(z)\\ &+ i(\nabla^2\theta)F_{\mathrm{R}}(z) + (\nabla\theta)^2 F_{\mathrm{R}}(z)\\ &- k_0^2\frac{n_o^2+n_e^2}{2}F_{\mathrm{R}}(z) - k_0^2\frac{n_o^2-n_e^2}{2}F_{\mathrm{L}}(z),\end{aligned} \tag{3.30}$$

$$\begin{aligned}\partial_z^2 F_{\mathrm{L}}(z) + 2i(\partial_z\theta)\partial_z F_{\mathrm{L}}(z) = &-\nabla_\perp^2 F_{\mathrm{L}}(z) - 2i(\nabla_\perp\theta)\cdot\nabla_\perp F_{\mathrm{L}}(z)\\ &- i(\nabla^2\theta)F_{\mathrm{L}}(z) + (\nabla\theta)^2 F_{\mathrm{L}}(z)\\ &- k_0^2\frac{n_o^2+n_e^2}{2}F_{\mathrm{L}}(z) - k_0^2\frac{n_o^2-n_e^2}{2}F_{\mathrm{R}}(z).\end{aligned} \tag{3.31}$$

To perform SVEA, we extract and separate the fast dynamics from $F_{\mathrm{R}}(z)$ and $F_{\mathrm{L}}(z)$, i.e. the dynamics over the small length scale λ . The electromagnetic wavefunction $\boldsymbol{\psi}_{\mathrm{oe}}(z)$ can also be expressed as

$$\boldsymbol{\psi}_{\mathrm{oe}}(z) = F_{\mathrm{R}}\psi_{\mathrm{R}}(z) + F_{\mathrm{L}}\psi_{\mathrm{L}}(z), \tag{3.32}$$

where $\psi_{\mathrm{R,L}}(z) = \dfrac{\psi_{\mathrm{o}}(z) \pm \psi_{\mathrm{e}}(z)}{\sqrt{2}}$. The dynamics of this wavefunction in the limit when $\lambda \ll \Lambda$ is given by (see Eq. (3.22) in the appendix)

$$\psi_{\mathrm{o}}(z) = e^{ik_0 n_{\mathrm{o}} z}\psi_{\mathrm{o}} + \mathcal{O}(\lambda/\Lambda), \tag{3.33}$$

$$\psi_{\mathrm{e}}(z) = e^{ik_0 n_{\mathrm{e}} z}\psi_{\mathrm{e}} + \mathcal{O}(\lambda/\Lambda). \tag{3.34}$$

Inserting this into Eq. (3.32) and comparing with Eq. (3.29) we find that

$$\begin{pmatrix} F_{\mathrm{R}}(z) \\ F_{\mathrm{L}}(z) \end{pmatrix} = \left[e^{ik_0\bar{n}z} \begin{pmatrix} \cos\frac{\pi z}{\Lambda} & -i\sin\frac{\pi z}{\Lambda} \\ -i\sin\frac{\pi z}{\Lambda} & \cos\frac{\pi z}{\Lambda} \end{pmatrix} (1 + \mathcal{O}(Z)) \right] \begin{pmatrix} F_{\mathrm{R}} \\ F_{\mathrm{L}} \end{pmatrix}, \tag{3.35}$$

where $Z = \varepsilon_2 z$ is the slow variable along the propagation direction in this regime. Thus, the amplitudes' dynamics include two different length scales λ and Λ. If we assume Λ to be comparable with the Rayleigh length, we can consider that the fast dynamics is only given by the exponential in the first term , which leads to the following separation:

$$\begin{pmatrix} F_{\mathrm{R}}(z) \\ F_{\mathrm{L}}(z) \end{pmatrix} = e^{ik_0\bar{n}z} \begin{pmatrix} F_{\mathrm{R}}(Z) \\ F_{\mathrm{L}}(Z) \end{pmatrix}. \tag{3.36}$$

By Inserting this into Eqs. (3.30) and (3.31) we get to the following coupled equations of motion:

$$\begin{aligned} &- k_0^2\bar{n}^2 F_{\mathrm{R,L}}(Z) + 2ik_0\bar{n}\partial_Z F_{\mathrm{R,L}}(Z) + \partial_Z^2 F_{\mathrm{R,L}}(Z) \\ &\mp 2i\partial_Z\theta\left[\partial_Z F_{\mathrm{R,L}}(Z) + ik_0\bar{n}F_{\mathrm{R,L}}(Z)\right] = -\left(\nabla_\perp \mp i\nabla_\perp\theta\right)^2 F_{\mathrm{R,L}}(Z) \\ &- k_0^2\left[\bar{n}^2 + (\Delta n/2)^2\right] F_{\mathrm{R,L}}(Z) - k_0^2\bar{n}\Delta n F_{\mathrm{L,R}}(Z) \end{aligned} \tag{3.37}$$

Now, after introducing the fast and slow variables the SVEA can be performed by considering $\lambda \ll \Lambda, Z_{\mathrm{R}}$. It follows that

$$i\partial_Z F_{\mathrm{R}}(Z) = -\frac{1}{2\bar{n}k_0}\left(\nabla_\perp - i\nabla_\perp\theta\right)^2 F_{\mathrm{R}}(Z) - \partial_Z\theta F_{\mathrm{R}}(Z) - \frac{\pi}{\Lambda}F_{\mathrm{L}}(Z), \tag{3.38}$$

$$i\partial_Z F_{\mathrm{L}}(Z) = -\frac{1}{2\bar{n}k_0}\left(\nabla_\perp + i\nabla_\perp\theta\right)^2 F_{\mathrm{L}}(Z) + \partial_Z\theta F_{\mathrm{L}}(Z) - \frac{\pi}{\Lambda}F_{\mathrm{R}}(Z). \tag{3.39}$$

So in this case, we find the following expressions for the scaler potential and the gauge field:

$$\mathbf{A} = -i\nabla_\perp\theta\sigma_z, \tag{3.40}$$

$$\mathbf{V} = -\nabla_Z\theta\sigma_z - \frac{\pi}{\Lambda}\sigma_x. \tag{3.41}$$

Table 3.1: Summary of SVEA

	Fast scales	Slow scales	**V**	**A**
case I	λ, Λ	Z_{R}	$-(\partial_z\theta)\mathbf{S}(z) + \frac{1}{2\bar{n}k_0}\left[i(\partial_z^2\theta)\mathbf{S}(z) + (\partial_z\theta)^2\right] \overset{\frac{w}{Z_\theta}\ll 1}{=\!=\!=} -(\partial_z\theta)\mathbf{S}(z)$	$-(\nabla_\perp\theta)\mathbf{S}(z)$
case II	λ	Λ, Z_{R}	$\nabla_Z\theta\sigma_z - \frac{\pi}{\Lambda}\sigma_x$	$-i\nabla_\perp\theta\sigma_z$
case III	λ, Z_{R}	Λ	$--$	$--$

Low birefringence limit

The third physically relevant regime occurs when the birefringence vanishes. According to Eq.(3.6), this implies that the beat length, Λ is slow even with respect to the Rayleigh length. Thus, we would expect that the polarization dynamics does not affect the defocusing of light and hence its confinement within a waveguiding region. In this sense, this limit is not of interest in the waveguiding regime we are looking for. In other words, the variations of the nematic texture in this regime are so slow that they do not have an effect on the light ray's propagation and its expansion.

We conclude this section by summing up the discussion on the fast and slow scales in the Table. 3.1.

3.5.3 Floquet theory for a periodically driven system

The physical systems we study here are examples of periodically driven systems which are vastly studied in the context of Floquet theory. A periodically driven quantum mechanical system is described by a time-periodic Hamiltonian $H(t+T) = H(t)$ [61, 79]. However, the examples of such systems are not restricted to quantum mechanics. Namely, the z-periodic photonic liquid crystal system that we study is described by an effective paraxial equation, Eq. 3.14, that can be mapped to a time-periodic Schrödinger equation. Here we review some of the most basic ideas behind the Floquet theory and study its application in our system.

The time-dependent Schrodinger equation $i\partial_t \left|\phi(t)\right\rangle = H(t)\left|\phi(t)\right\rangle$ is solved as follows;

$$\left|\phi(t)\right\rangle = U(t,t_0)\left|\phi(t_0)\right\rangle, \tag{3.42}$$

where the evolution operator is given by the following time-ordered integral

$$U(t,t_0) = \mathcal{T}\exp\left(i\int_{t_0}^{t} H(t')dt'\right). \tag{3.43}$$

For a time periodic Hamiltonian the evolution operator is also periodic, namely

$$U(t_2, t_1) = U(t_2 + T, t_1 + T), \tag{3.44}$$

and thus, for $\tau \in [0, T]$ and for any integer n

$$U(\tau + nT) = U(\tau) \left[U(T)\right]^n, \tag{3.45}$$

where we set the initial time t_0 to zero. Therefore, the full evolution of the wavefuction can be characterized by the evolution operator in one time period. Particularly for large time scales the wavefunction time evolution is in the stroboscopic picture given by the set of wavefunction at the time periods $\{|\phi(nT)\rangle = [U(T)]^n |\phi(0)\rangle\}|_n$. The advantage of using the stroboscopic picture is that it contains the relevant information about the wavefunction dynamics for time scales much larger than the Floquet period T. For example, although the time dependence of the Hamiltonian does not allow for an eigenmode of the full evolution operator, in the stroboscopic picture the eigenmodes of the evolution operator over one time period are the eigenstates of the full evolution.

Furthermore, for a system described by a Hermitian Hamiltonian, $U(T)$ is a unitary operator and thus its eigenvalues are given by $e^{i\beta T}$, where β is called quasi-energy and is defined modulo $2\pi/T$. Therefore, the stroboscopic evolution of the eigenstate u is given by

$$|\phi(nT)\rangle = e^{in\beta T} |\phi\rangle . \tag{3.46}$$

In the photonic system under study, these eigenstates are associated with the guided modes of the system. Also, the eigenvalues are quasi-momenta in this case, as the effective time is actually of a spatial origin in this problem and the periodicity of the system is set by the length Λ. Note that the validity of this result for the photonic system depends on the condition that the dynamics of the wavefunction inside a Floquet period is small enough that the effective paraxial equation is always a valid description. This condition is satisfied in the adiabatic regime where the Floquet period is much smaller than the Rayleigh length, that is given by Eq. 3.4. This result implies that there are higher order guided modes with non-Gaussian distributions which are guided in a non-uniform uniaxial media, as shown by Fig. 3.1.

Representation in the Sambe space

We saw above that to obtain the guided modes of a periodic liquid crystal structure we need to solve the diagonalization problem

$$U(t_0 + T, t_0) \left|\phi(t_0)\right\rangle = e^{i\beta T} \left|\phi(t_0)\right\rangle . \tag{3.47}$$

Since $U(t_0 + T, t_0)$ is a unitary operator, its eigenvalues are all located on the circumference of the unit circle. It thus become likely that for high resolution simulation boxes, the different modes of the system have very close quasi-energies and become practically degenerate. A numerical scheme then can become unstable due to these artificial degenerate spaces. To solve this issue, we use the Floquet Hamiltonian's Sambe-space representation, which is a time-independent equivalent problem to solving the time-periodic quantum-mechanical system [176].

This method requires writing the Hamiltonian in the Sambe space, which is an enlarged space composed of the sidebands of the Floqeut Hamiltonian [50]. The eigenvalue problem above then can be expressed in this space as

$$\mathcal{H}^S \left|\mathcal{U}\right\rangle = \beta \left|\mathcal{U}\right\rangle , \tag{3.48}$$

where $\mathcal{H}^S$ is the Sambe Hamiltonian whose blocks are given by the Fourier components of the Floquet Hamiltonian $H(t) - i\partial_t$ as

$$\mathcal{H}^S_{IJ} = H^{(I-J)} - I\delta_{I,J}\omega, \tag{3.49}$$

where $I, J \in \mathbb{Z}$, $H^{(p)}$ is the pth Fourier harmonic of the Hamiltonian, $\delta_{I,J}$ is the Kronecker delta, and ω is the drive frequency. The eigenstate $\left|\mathcal{U}\right\rangle$ is also obtained by the column stacking of the Fourier components of the periodized wavefunctin $\left|u\right\rangle$[♠]:

$$\left|\mathcal{U}\right\rangle = \begin{pmatrix} \vdots \\ \left|u\right\rangle^{(I-1)} \\ \left|u\right\rangle^{(I)} \\ \left|u\right\rangle^{(I+1)} \\ \vdots \end{pmatrix} . \tag{3.50}$$

[♠]This can be obtained from a Floquet eigenstate as $\left|u_\alpha(t)\right\rangle = V(t)\left|\phi_\alpha\right\rangle$, where $V(t)$ is the short-term (within a Floquet period) propagator.

Note that the eigenvalues of this method can have arbitrary norms that solves the issue that we described above: the two eigenvalues β_0 and $\beta_0 + \epsilon + 2n\pi$ where ϵ is small with respect to the resolution of the diagonalization code are in this method well separated from each other, while in the previous method they were pointing to very close points on the unit circle which could lead to accidental degeneracies.

We skip the details of the calculations of $\mathcal{H}^S$ for the various cases that we consider in this thesis. We solve the time-independent problem above numerically using usual diagonalization methods. To find the lowest order guided modes, we look for the maximally spatially localized modes that are obtained from the eigenmodes of the Sambe Hamiltonian.